

Thermal and grinding performance of 3D printed compliance grinding tools with rotary-enhanced heat transfer structure

Mingcong Li¹, Shaoze Yan², KaiFan Zhang¹, Wenxi Wang^{1,3}, Lai Zou^{1,3}, Yun Huang^{1,3}

¹College of Mechanical and Vehicle Engineering, Chongqing University, No. 174, Shazhengjie, Shapingba, Chongqing, 400044, P.R. China

²Chongqing University-University of Cincinnati Joint Co-op Institute, Chongqing University, No. 55, University Town South Road, Shapingba, Chongqing, 400044, P.R. China

³State Key Laboratory of Mechanical Transmissions for Advanced Equipment, Chongqing University, No. 174, Shazhengjie, Shapingba, Chongqing, 400044, P.R. China

Abstract

Compliance ball-head (BE) grinding tools show promise for precision grinding of complex curved components in narrow areas, represented by integral discs. However, the grinding process generates significant heat in the grinding zone, which can limit the tool's service life and performance. To address this issue, a rotary-enhanced heat transfer (RHET) structure based on turbine blade was designed in this study. Numerical simulations were used to demonstrate the heat transfer mechanism of the tool. The tools were structured using multi jet fusion and their grinding performance was compared to conventional structures through robot-assisted grinding of titanium plates. The results indicated that the REHT improved the heat transfer capability of the BE by introducing high momentum fluids and increasing the pressure at the inner wall. The REHT structure resulted in a reduction of the grinding temperature by over 19.84%, leading to a tool life extension of more than 40%. Furthermore, compliant grinding tools with REHT resulted in a higher cumulative material removal alongside lower and more consistent surface roughness (Ra).

Keywords: Flow behavior; grinding performance; enhanced heat transfer

1. Introduction

Complex structural parts for applications in aerospace and national defense present a trend towards miniaturization, structural complexity and increasing machining requirement [1]. Difficult-to-machine materials such as titanium alloys are used to manufacture these components, which require excellent structural stability and reliability to overcome the tough working conditions in service [2]. Effective control of machining accuracy and surface quality is one of the major challenges in precision grinding and polishing of these components. Compliance grinding, such as belt grinding, has been widely used for precision grinding curved component with non-interference-prone areas, like blade profiles [3]. Nevertheless, the machining of narrow and irregular interference-prone areas such as blade roots and runner surfaces, where interleaf space is less than 20 mm, the minimum curvature radius of ground surface is less than 2 mm and the interference-surface curvature varies greatly, is still largely dependent on manual work by skilled operators. To avoid interference caused by the process of intricate structural components, ball-end grinding tools with small size are used [5][6].

The complex structure of the component results in a narrow space, which makes the grinding process highly susceptible to interference. This limitation restricts the size of the tool and the amount of coolant that can be used. Additionally, the variable position of the tool during the process presents a challenge for delivering precise cooling (Figure 1(a)). Furthermore, the grinding tool creates an air barrier on the surface during rotational movement (Figure 1(b)), causing a difference in the air flow rate and preventing proper cooling in the actual grinding area. If higher grinding efficiencies are

desired, increasing the rotating speed further will amplify the cooling challenge (Figure 1(c)).

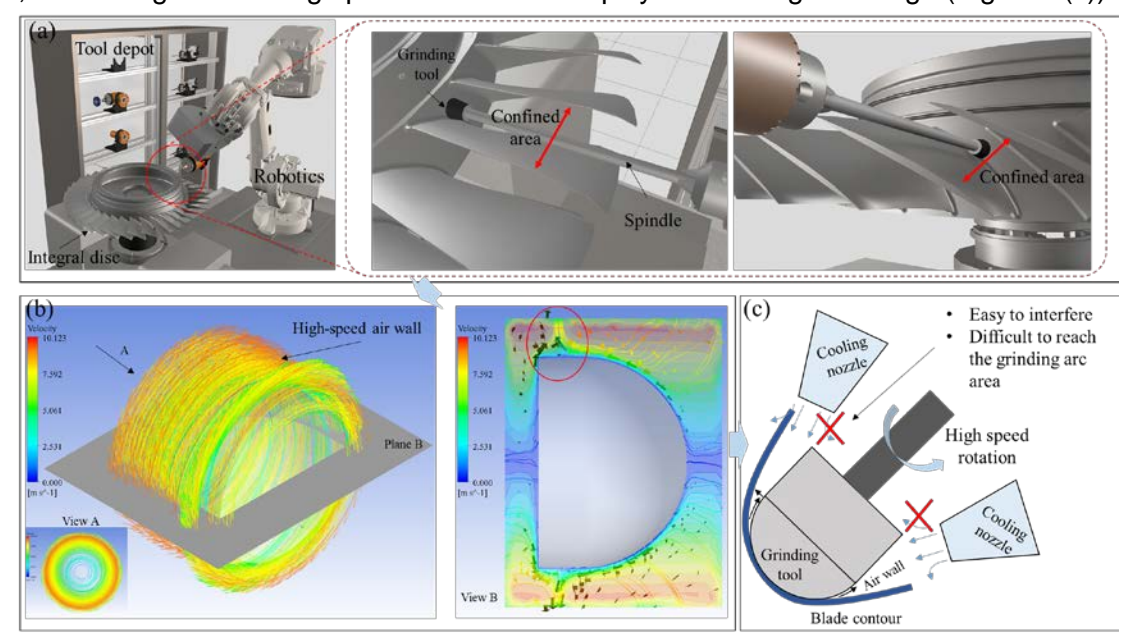


Figure 1 – (a) Interference-prone areas due to complex structural components, such as integral discs, (b) air walls formed by BE rotation, (c) difficulty in cooling due to service conditions.

Advanced heat transfer technologies, such as including liquid nitrogen cooling [7], heat pipe technology [8], and internal cooling [9][10] and low-temperature cold air technology [11] have been widely investigated. Liquid nitrogen might impact the ground surface's quality in a negative manner [12]. The use of heat pipe technology and internal runners is limited by manufacturing conditions and costs, making it challenging to apply them to small grinding tools with diameters of less than 15mm. On the other hand, cold air jet technology has been effective in preventing chip adherence and suppressing grinding heat accumulation [13]. However, delivering cold air accurately into the grinding zone of a variable position tool is a challenge within the constraints of complex structural components. It is evident that simply increasing the air power of the cold air injection is an inefficient approach, which contradicts the principles of energy efficiency and sustainable manufacturing strategies.

2. Numerical and Experimental

2.1 Modeling and Numerical Analysis

2.1.1 Design of Tool with RHET

Aero-engine accelerates and pressurizes large amounts of air into the combustion cavity, producing thrust that forces the aircraft forward [14]. Additionally, the mature free-form modeling method of the blade facilitates further optimization of the enhanced heat transfer structure in subsequent studies. For this purpose, turbine blades with were selected as prototypes of rotationally enhanced heat transfer structures for BE. Table 1 shows the parameters of the REHT. The 3D printing technique was carefully chosen to prepare the BE substrate, considering the manufacturability of preparing flexible materials with complex structures in small sizes. To ensure printability, the large-size blade needs to be scaled and thickened first to meet the minimum wall thickness (>0.8 mm) for printing, as shown in Figure 2(a). Based on a typical aircraft blade, the BE model with REHT is shown in Figure 2 (b).

Table 1 – Parameters of the blades.

Parameters	TB-BE
Chord length (mm)	3.62
Inlet geometry angle ($^{\circ}$)	17.7
Maximum thickness (mm)	1.38
Width to height ratio	1.03

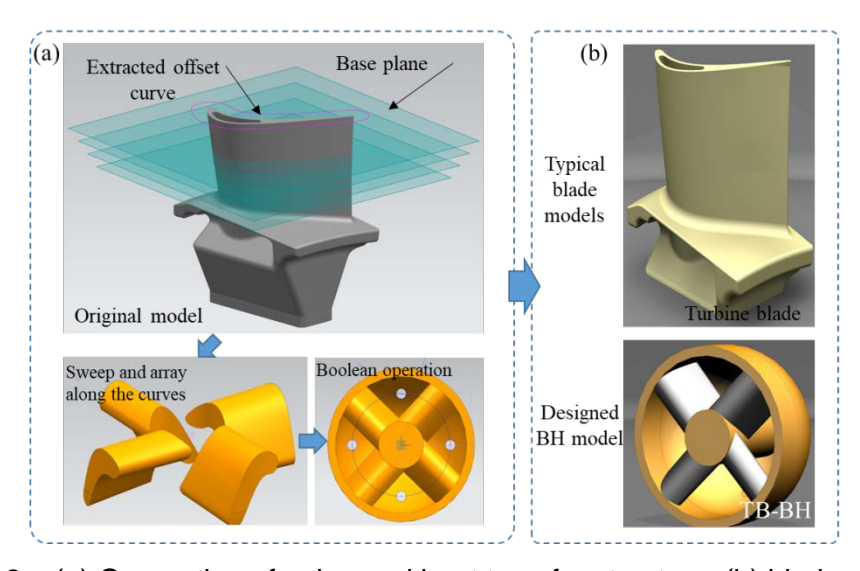


Figure 2 – (a) Generation of enhanced heat transfer structure, (b) blade and BEs.

Table 2 – Details of BEs

. 6.6.6	
Code	Structure
NB-BE	Cavity-based
TB-BE	Turbine blade based

2.1.2 Numerical Methodology

To solve the overall flow-temperature characteristics of BE, a numerical analysis method is performed using Ansys Fluent 2022R1. The governing equations required for numerical calculations as follows.

The continuity and RANS equations are given by the following equation:

$$\frac{\partial}{\partial x_i}(u_i) = 0 \tag{1}$$

$$\frac{\partial}{\partial x_i}(u_i) = 0$$

$$\frac{\partial}{\partial x_j}(\bar{u}_i\bar{u}_j) = -\frac{1}{p}\frac{\partial}{\partial x_i}(\bar{p}) + \frac{\partial}{\partial x_j}\left(\mu\frac{\partial\bar{u}_i}{\partial x_j} - \overline{u'_ju'_i}\right)$$
(2)

where \bar{u}_i and u'_i are the time-averaged and fluctuating velocity components in three directions, respectively. p and μ are the density and dynamic viscosity. \bar{p} is the time-averaged static pressure, and x_i is the spatial coordinates.

The energy equation is:

$$\frac{\partial}{\partial x_j} \left(u_i c_p T \right) = k \frac{\partial^2 T}{\partial x_j^2} \tag{3}$$

where c_p , k, and T represent the specific heat, thermal conductivity, and temperature.

The mathematical expression for the standard k-ε turbulence model is given by the following equation:

$$\frac{\partial}{\partial x_j} \left(u_i c_p T \right) = k \frac{\partial^2 T}{\partial x_j^2} \tag{4}$$

where c_p , k, and T represent the specific heat, thermal conductivity, and temperature.

the Standard k-ε turbulence model are presented below:

$$\frac{\partial \rho u_j k}{\partial x_i} = \rho P - \rho \varepsilon + \frac{\partial}{\partial x_i} \left[\left(\mu + \frac{\mu_t}{\sigma_k} \right) \frac{\partial k}{\partial x_i} \right] \tag{5}$$

$$\frac{\partial \rho u_i \varepsilon}{\partial x_i} = C_{\varepsilon 1} \frac{\rho P \varepsilon}{k} - C \varepsilon 2 \frac{\rho \varepsilon^2}{k} + \frac{\partial}{\partial x_i} \left[\left(\mu + \frac{\mu_t}{\sigma_{\varepsilon}} \right) \frac{\partial \varepsilon}{\partial x_i} \right]$$
 (6)

$$P = \frac{\mu_t}{\rho} C_{\varepsilon 1} \left(\frac{\partial u_j}{\partial x_i} + \frac{\partial u_i}{\partial x_j} \right) \frac{\partial u_j}{\partial x_i}$$
 (7)

$$\mu_t = \frac{C_\mu \rho k^2}{\varepsilon} \tag{4}$$

where k is the turbulent kinetic energy and ε is the turbulent kinetic energy dissipation rate.

Steady-state calculations employ the multi-reference frame model (MRF), a method that has been accurately and efficiently validated in numerous published journal papers [15]. As all regions of the BE may come into contact with the workpiece and generate grinding heat under working conditions, the entire BE surface was treated as a heating wall. The wall surface was uniformly heated to a temperature of 200°C, and the wall thickness was set to 1mm. The interface for data transfer is established at the surface between the BE and the rotating area. The inlet and outlet boundaries are defined as velocity inlet and free outflow, respectively. The pressure–velocity coupling is conducted utilizing the coupled scheme with a standard wall function. The inlet and outlet boundaries are defined as velocity inlet and velocity outflow, respectively. Grid independence is employed to find the optimal solution that balances accuracy and computational time, yielding precise results in the shortest calculation time. Ultimately, the model comprises 2.21 million meshes, at which point the average pressure and velocity exhibit changes of less than 1%.

2.1.3 Visualization of BE – Effects of Rotational Direction And Speed

The reference plane-ZX (RFZX) plane was visualized to observe the Flow behavior of BE inner cavity. The velocity vectors, contour plots of pressure, and distribution of turbulent kinetic energy for different BEs in clockwise and counterclockwise rotations are shown in Figure 3, respectively. Due to the rotational action of the BE, air flows in from the inner side of its inner cavity and out from the outer side of the inner cavity. When the CB-BE are rotated clockwise, a distinct vortex is formed in the inner cavity, as depicted in Figure 4(a) and Figure 3(b). This difference may be attributed to the variation in blade mounting angles. The blades act as turbulence generators, enhancing airflow convection in the inner cavity. The formation, propagation, and destruction of vortices facilitate enhanced heat transfer [16]. Furthermore, the enhanced heat transfer structure causes the air to stagnate near the outer wall of the inner cavity, creating a high-pressure region. This region induces more fluid flow, thereby promoting heat transfer. BEs with RHET generate greater turbulent kinetic energy (TKE) within the inner cavity, consistent with the vortex position. On the other hand, BEs without vanes show no significant difference in pressure distribution (Figure 3(a)) and exhibit lower turbulent kinetic energy only near the wall (Figure 3(b)), indicating weaker heat transfer.

When the TB-BE rotate clockwise the temperature of the surface and inner wall is lower in the inner cavities. The rotation direction does not change the average surface temperature in the case of BE without RHET. However, the surface-averaged temperatures of both the surface and inner wall experienced a considerable decrease in the TB-BE, with reductions up to 13.80°C and 27.78°C, respectively. This cooling effect is attributed to the air entrainment caused by the pressure difference inside the inner cavity, which is amplified by the enhanced heat transfer structure when the TB-BE is rotated clockwise. This results in increased air intake volume and the generation of a wider range of high-momentum regions, thereby enhancing heat transfer.

The reduction in average surface and inner wall temperature increases with the rotating speed. The TB-BE demonstrates the stronger heat transfer capability compared to the conventional solid structure (Figure 4 (b)). Furthermore, the temperature homogeneity of the BE surface and inner wall improves with increasing rotational speed (Figure 5 (c)). The temperature distribution along the x-axis shows a roughly circular pattern, with lower temperatures at the top and bottom of the BE and

higher temperatures in the center. This is attributed to the discontinuity of the vortex in this region. Future studies will focus on controlling the location of vortex generation to further direct the cooling towards specific zones.

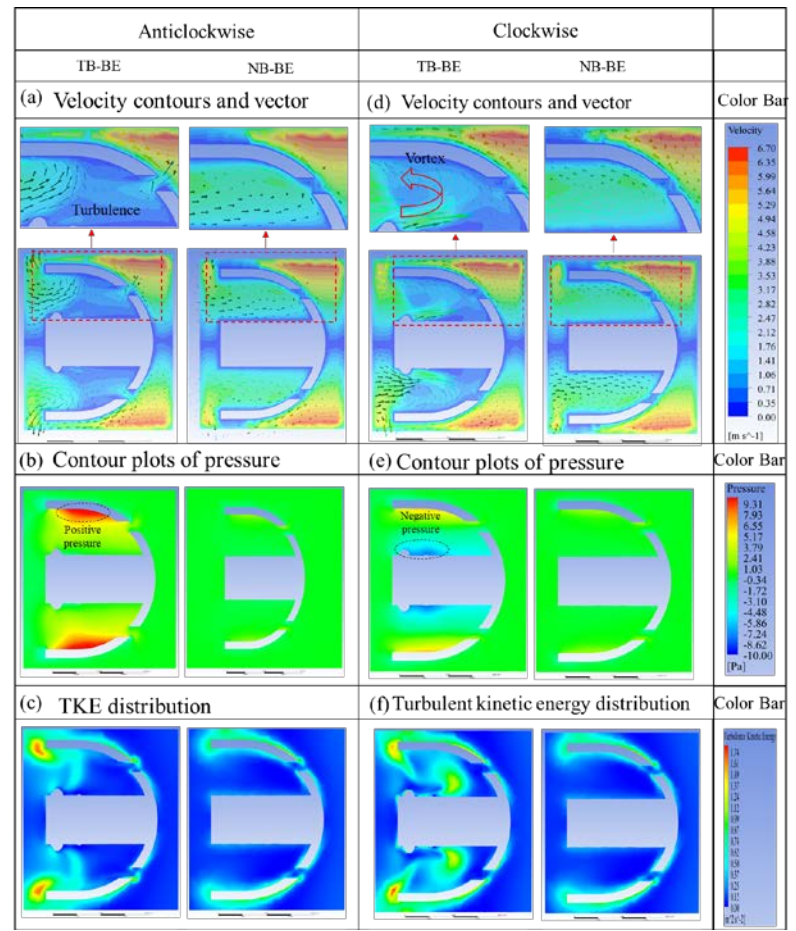


Figure 3 – Visualize the flow characteristics in RFZX with different BEs in different rotational directions

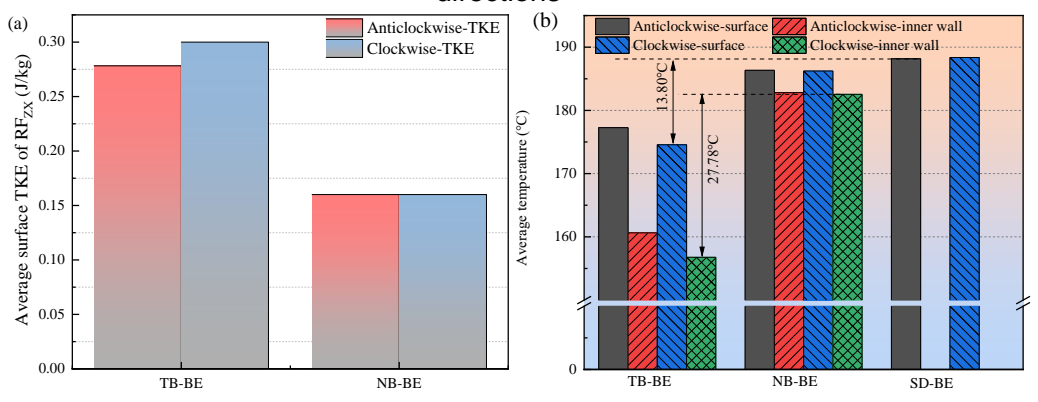
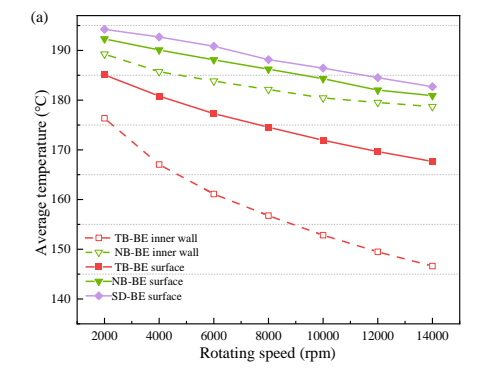


Figure 4 – (a) Average surface TKE of RFZX and (b) average surface temperature with different BEs in different rotational directions



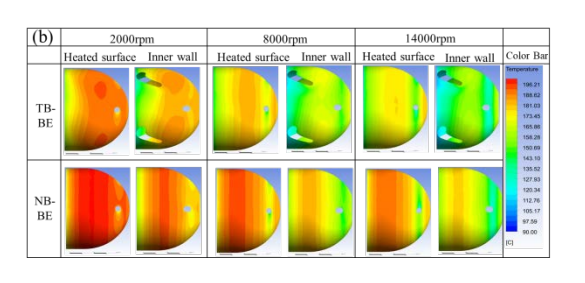


Figure 5 – (a) Average surface temperature and (b) surface temperature distribution with different BEs in different rotational speed

2.2 Experimental Procedures

A robotic grinding platform, as shown in Figure 6 (b) and Figure 6 (c), was used for the grinding tests. This platform is composed of an industrial robot (FANUC, M-710iC/50), force sensor (KUNWEI, R75B), grinding spindle (Haozhi Industrial, DGZX-08040), cold air gun (AIRSTE, CAG 2106), and thermal imaging infrared cameras (FLIR, E6-XT). The robot executed the trajectory operation with high programming flexibility [17]. The end effector of the robot had a strain force sensor to measure the grinding force at a frequency of 1000hz with 0.1%FS accuracy. The grinding spindle with the hole full beating less than 0.002mm, spindle vibration less than 1mm/s. Generation of forced cooling air through vortex tubes with a cooling capacity of 101Kcal/H. Throughout the grinding process, the thermal imaging infrared cameras, featuring an expanded temperature range from -20 °C to 550 °C and accuracy of ±2%, were used to records the grinding heat at a fixed position and determine the maximum temperature within the frame as the grinding temperature. Titanium alloys (TC4, 100mm×100mm×10mm) were selected for machining to assess the performance of BEs, employing the parameters described in Table 3.

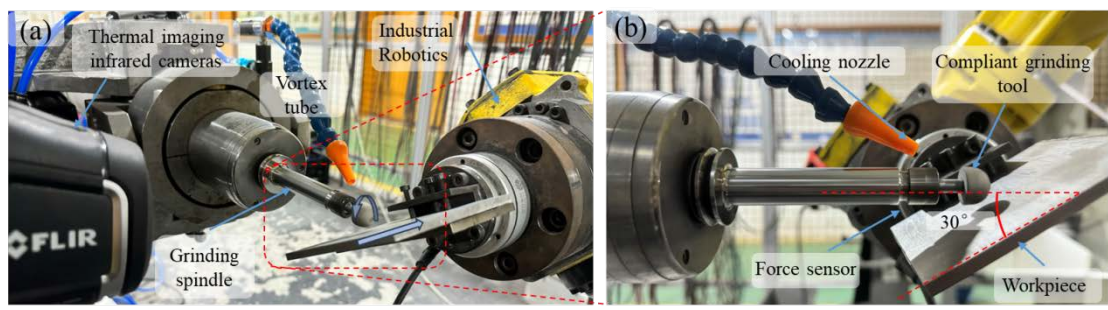


Figure 6 – Grinding experimental set-up

Table 3 – Parameters of the experiment process.

Table 6 Talameters of the experiment process.	
Parameters	Value
grit size	400 (Us mesh)
Rotating speed $^{\it \omega}$ (rpm)	3000,4500,6000,7500,9000,1050,12000
Feed rate Vw (mm/s)	0.3, 1
Normal force Fn (N)	3, 5
Workpiece material	TC4, HRC 30

3. Experimental Results And Discussion

The impact of REHT on the grinding performance of BE tools was investigated by continuously grinding (Figure 7). Initially, all the BE tools experienced a significant temperature rise due to the interaction between the sharp grits and the workpiece, reaching 100°C within 20s. The highest grinding temperatures were observed in the SD-BE tool, with temperatures exceeding 140°C from 55s to 100s. The intense accumulation of localized grinding heat caused the flexible material to melt and adhere to the tool surface, hindering the abrasive grits from effectively removing material. Consequently, the material removal capability of the SD-BE tool sharply decreased after 140s (Figure 7 (b)). The NB-BE tool initially had the lowest grinding temperature for the first 50s, but due to the accumulation of localized temperatures, its grinding temperature gradually increased and reached 136°C in 190s. On average, its temperature was 114.9°C, second only to the average grinding temperature of the SD-BE tool. However, its weak rigidity under the hollow structure resulted in significantly lower material removal compared to other BE tools. In contrast, the BE with REHT maintained a relatively stable grinding temperature and material removal capacity throughout the continuous grinding process, while also maintaining favorable surface quality.

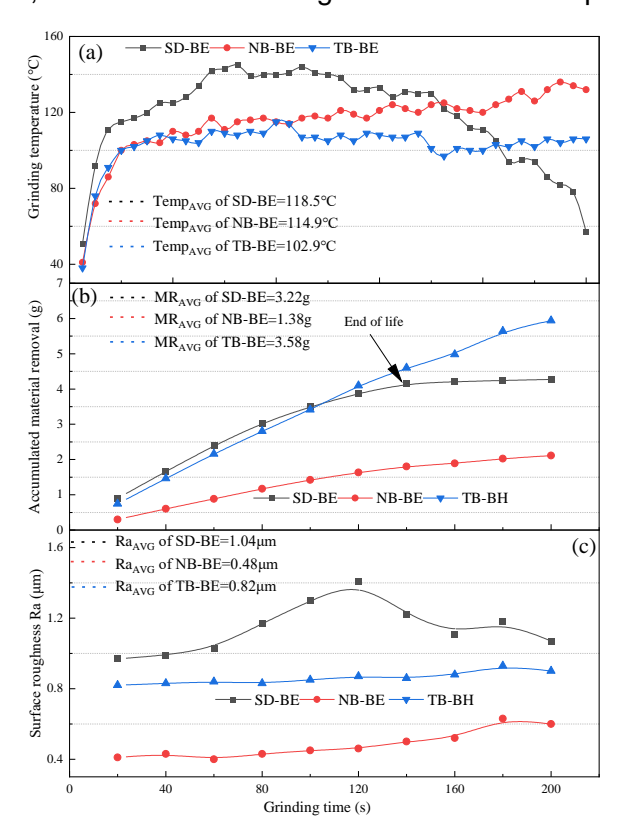


Figure 7 – (a) Grinding temperature, (b) accumulated material removal and (c) Ra of BE tools undergoing continuous grinding

Aligns with the roughness results, ground surface texture of SD-BE and NB-BE tools tends to become rougher as the increased plastic flow with the continuous grinding (Figure 8). Whereas, the ground surface texture of TB-BE tools maintains a favorable consistency. In the initial stage of grinding (grinding time=20s), SD-BE and TB-BE tools all produce continuous scratches and plastic flows on the ground surface, with TB-BE generating slightly more plastic flow. In contrast, NB-BE generates intermittent scratches and plastic flows. As the grinding progresses and the temperature rises (grinding time=100s), the continuous scratches and plastic flows on the ground surface of the SD-BE tool become intermittent, while more plastic flow appears on the ground surface of the NB-BE tool. The grinding surfaces of TB-BE tools remain smoother with less plastic flow. In the final stage of grinding (grinding time=200s), both SD-BE and NB-BE surfaces show a large amount of plastic flow and shallower scratch depths. Due to grit wear, the plastic flow and scratches on the ground surfaces of TB-BE tools also become intermittent, but still maintain relatively smoother surfaces, similar to the early stage of the grinding process.

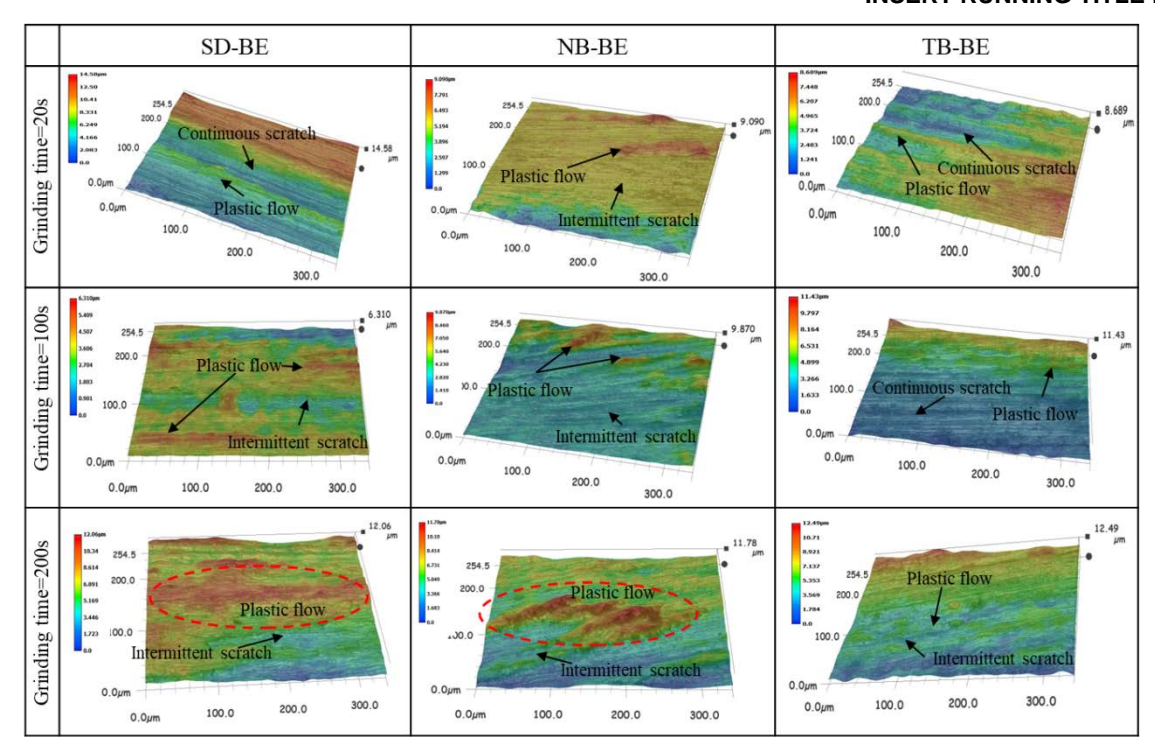


Figure 8 – Surface morphology of ground surface of BE tools undergoing continuous grinding

There are two main failure forms of the abrasive layer during continuous grinding. One form is the adhesion of the flexible substrate caused by intense grinding heat, while the other form is the fracture of the abrasive layer due to alternating stress (Figure 9). The latter form is unavoidable during continuous grinding, but the former significantly reduces the tool's lifespan. After experiencing 200s continuous grinding, different BE tools exhibited varying degrees of fall-off in their abrasive layers, with the SD-BE tool experiencing the most pronounced fall-off. Additionally, a ring-like adhesion was observed on the tool surface of the SD-BE tool. This adhesion occurred when the flexible matrix inside the tool melted due to intense temperature accumulation and adhered to the tool surface due to the centrifugal force of high-speed rotation. The adhesion reduced the grit protrusion height and weakened the cutting ability. Only a few adhesions were noticed on the NB-SD tool surface. Although the weak grinding capacity under weak rigidity does not cause high grinding temperatures, its weak heat dissipation capacity leads to a continuous rise in local temperature during continuous grinding, resulting in inevitable flexible material adhesion. The main failure form of TB-BE tools was abrasive layer fall-off. These tools have an enhanced heat transfer structure that effectively exchanges cold air with the high localized heat in the grinding zone, thereby alleviating the adhesion of the flexible substrate.

The mechanism of improved heat transfer by the internal blade structure can be summarized in Figure 10. The internal blade draws in external cold air, creating a high momentum and high-pressure zone in the tool's cavity. This cools the tool's inner wall and facilitates heat transfer. The pressurized cold air is then injected into the hot surface of the workpiece through an opening in the bottom of the tool, increasing the surface flow rate and further enhancing heat transfer. Finally, heat is expelled through enhanced chip removal, allowing it to be carried away by the chips instead of being retained on the workpiece or tool due to chip adhesion.

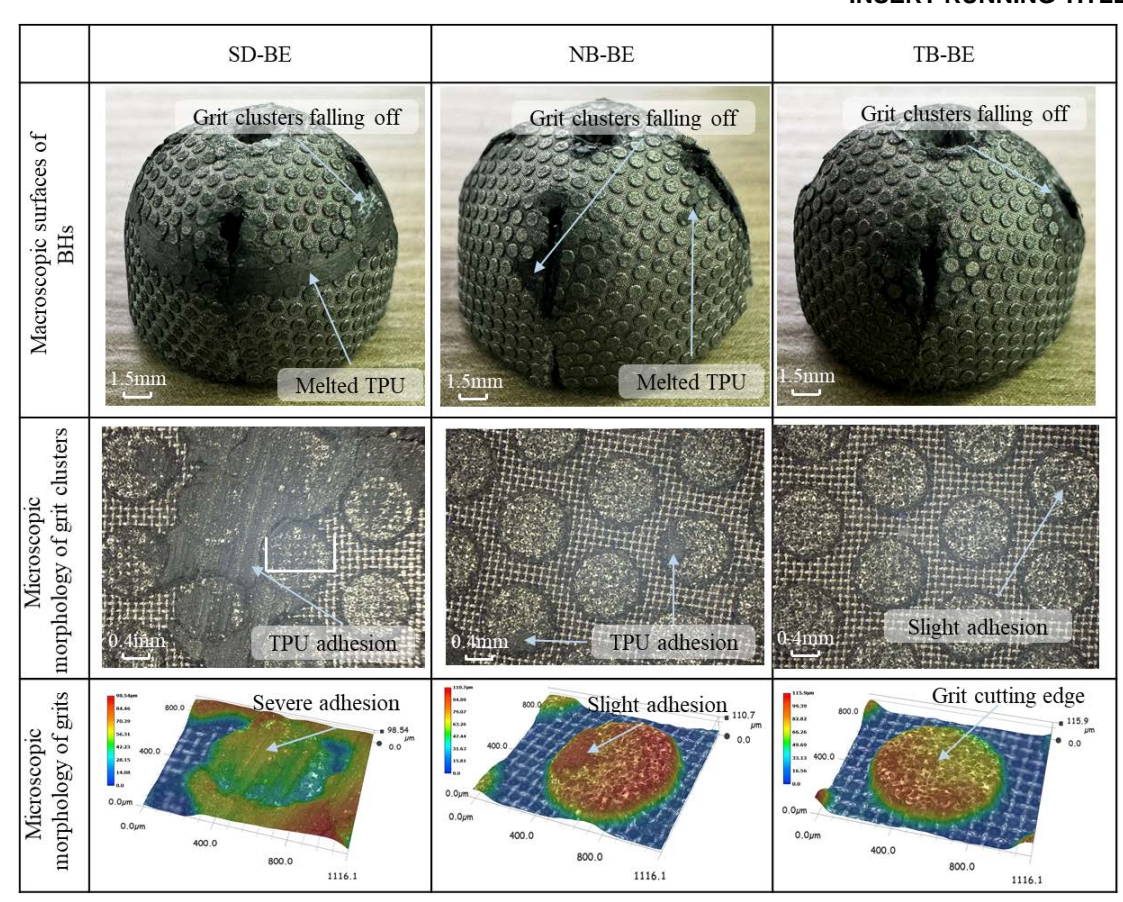


Figure 9 – Macroscopic and microscopic of abrasive layers after continuous grinding

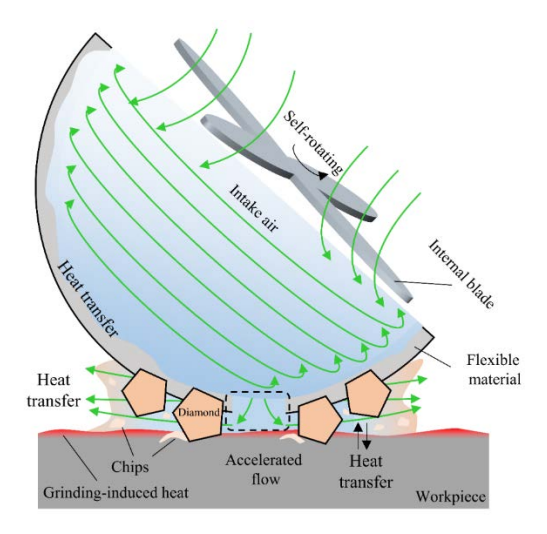


Figure 10 – Schematic diagram of enhanced tool heat transfer with RHET

4. Conclusion

In this study, the thermal performance BEs with RHET were analyzed by CFD based on three typical aero-engine blades. BH tools were prepared using MJF and their grinding performance was comparatively studied through grinding experiments. The main findings are as follows:

- 1. The blade-shaped structure produces a vortex in the inner cavity of BE and considerably enhances airflow convection within the cavity. The average surface temperature reduction rises with increasing rotating speed. The cooling effect is most significant in turbine blade-shaped structure.
- 2. The grinding temperature of conventional tools rises from 34.3°C to 100.5°C with increasing rotating speed. In contrast, the grinding temperature of blade-shaped structure tools ranges from 25.5°C to 71.5°C. The blade-shaped structure alleviates flexible material adhesion due to heat

accumulation during continuous grinding, resulting in over 40% longer tool life.

Acknowledgements

This study was supported by the China Postdoctoral Science Foundation (2023M740398) and the the Fundamental Research Funds for the Central Universities (No.2023CDJXY-024).

Reference

- [1] T.Z. Wang, H.N. Liu, C.Y. Wu, J. Chen, M.J. Chen, Interference and grinding characteristics in ultraprecision grinding of thin-walled complex structural component using a ball-end grinding wheel, Chin. J. Aeronaut. 34 (4) (2021) 192-207.
- [2] M.Y. Wang, X.Z. Chen, F.Z. Dai, K. Peng, R.A. Singh, S. Konovalov, Simulation of residual stress and micro-plastic deformation induced by laser shock imprinting on TC4 titanium alloy aero-engine blade, J. Mater. Res. Technol-JMRT, 26 (2023) 9419-9436.
- [3] C. Lv, L. Zou, Y. Huang, X.F. Liu, Z.R. Li, M.W. Gong, H. Li, A trajectory planning method on error compensation of residual height for aero-engine blades of robotic belt grinding, Chin. J. Aeronaut. 35 (4) (2022) 508-520.
- [4] B.X. Zhang, S.J. Wu, D.Z. Wang, S.L. Yang, F. Jiang, C.H. Li, A review of surface quality control technology for robotic abrasive belt grinding of aero-engine blades, Measurement, 220 (2023).
- [5] Y. Hwang, T. Kuriyagawa, S.-K. Lee, Wheel curve generation error of aspheric microgrinding in parallel grinding method, Int. J. Mach. Tools Manuf. 46 (15) (2006) 1929-1933.
- [6] T.Z. Wang, H.N. Liu, C.Y. Wu, J. Cheng, M.J. Chen, Three-dimensional modeling and theoretical investigation of grinding marks on the surface in small ball-end diamond wheel grinding, Int. J. Mech. Sci. 173 (2020) 105467.
- [7] F. Pusavec, D. Grguras, M. Koch, P. Krajnik, Cooling capability of liquid nitrogen and carbon dioxide in cryogenic milling, CIRP Ann-Manuf. Technol. 68 (1) (2019) 73-76.
- [8] N. Qian, Y.C. Fu, Y.W. Zhang, J.J. Chen, J.H. Xu, Experimental investigation of thermal performance of the oscillating heat pipe for the grinding wheel, Int. J. Heat Mass Transf. 136 (2019) 911-923.
- [9] Z.J. Du, F.L. Zhang, Q.S. Xu, Y.J. Huang, M.C. Li, H.P. Huang, C.Y. Wang, Y.M. Zhou, H.Q. Tang, Selective laser sintering and grinding performance of resin bond diamond grinding wheels with arrayed internal cooling holes, Ceram. Int. 45 (16) (2019) 20873-20881.
- [10]X.W. Xiao, Y.F. Jin, M.L. Chen, R.T. Peng, H. Tang, J.X. Gao, An internal cooling grinding wheel: From design to application, Chin. J. Aeronaut. 36 (11) (2023) 465-482.
- [11]A. Bagherzadeh, E. Budak, Investigation of machinability in turning of difficult-to-cut materials using a new cryogenic cooling approach, Tribol. Int. 119 (2018) 510-520.
- [12]P.P. Reddy, A. Ghosh, Some critical issues in cryo-grinding by a vitrified bonded alumina wheel using liquid nitrogen jet, J. Mater. Process. Technol. 229 (2016) 329-337.
- [13]T. Mizutani, U. Satake, T. Enomoto, A study on a cooling method for bone grinding using diamond bur for minimally invasive surgeries, Precis. Eng.-J. Int. Soc. Precis. Eng. Nanotechnol. 70 (2021) 155-163.
- [14]L.M. Amoo, On the design and structural analysis of jet engine fan blade structures, Prog. Aeosp. Sci. 60 (2013) 1-11.
- [15]Q.Y. Sai, H.D. Xu, J. Chen, J.T. Zhang, Experimental and numerical study on a new noise reduction design for a small axial fan, Appl. Acoust. 211 (2023) 109535.
- [16]C. Liang, Y. Rao, J.H. Luo, X.L. Luo, Experimental and Numerical Study of Turbulent Flow and Heat Transfer in a Wedge-shape d Channel with Guiding Pin Fins for Turbine Blade Trailing Edge Cooling, Int. J. Heat Mass Transf. 178 (2021) 121590.
- [17]Z.L. Wang, L. Zou, Y.L. Mu, W.X. Wang, Y. Huang, Region-based Force Control Strategy for Improving Profile Accuracy of Blade on 7-axis Linkage Robotic Grinding System, IEEE-ASME T. MECH. 99 (2023)

Copyright Statement

INSERT RUNNING TITLE HERE

The authors confirm that they, and/or their company or organization, hold copyright on all of the original material included in this paper. The authors also confirm that they have obtained permission, from the copyright holder of any third party material included in this paper, to publish it as part of their paper. The authors confirm that they give permission, or have obtained permission from the copyright holder of this paper, for the publication and distribution of this paper as part of the ICAS proceedings or as individual off-prints from the proceedings.